INORGANIC CHEMISTRY
FRONTIERS

RESEARCH ARTICLE

View Article Online
View Journal



Cite this: DOI: 10.1039/c9qi01223k

# Organic template-free synthesis of an open framework silicoaluminophosphate (SAPO) with high thermal stability and high ionic conductivity†

Dong Fan, [a] Nicolas Barrier, [b] Aurélie Vicente,[c] Jean-Pierre Gilson, [c] Simon Clevers, [d] Valérie Dupray,[e] Gérard Coquerel[d] and Valentin Valtchev *[c]

Received 23rd September 2019,
Accepted 11th November 2019

DOI: 10.1039/c9qi01223k

rsc.li/frontiers-inorganic

An open-framework silicoaluminophosphate (SAPO) material with a composition of $Cs_2(Al_{0.875}Si_{0.125})_4(P_{0.875}Si_{0.125}O_4)_4(HPO_4)$ was synthesized in an organic template-free cesium-containing system under hydrothermal conditions. The material was resolved to be isostructural with an open-framework aluminophosphate (AlPO) material AlPO-CJ19, which was previously synthesized using pyridine as the solvent and 2-aminopyridine as the organic template *via* a solvothermal route. The substitution of organic templates by alkaline cations not only makes the current synthesis protocol more favorable from an environmental point of view but also leads to a significantly improved thermal stability of this structure. The framework remained completely stable at a temperature of 510 °C. A high-temperature polymorph was discerned at a temperature higher than 540 °C, the structure of which is revealed to crystallize in the *P*1c1 space group. UV-vis results reveal that cobalt and copper cations could be readily incorporated through simple ion-exchange treatment. The conductivity of the material is $1.70 \times 10^{-4}$ S cm$^{-1}$ (293 K, 30% relative humidity) as revealed by the alternating current (A.C.) impedance spectroscopy analysis. This is the first report of the synthesis of a silicon-containing phase with an AlPO-CJ19 structure.

## Introduction

Open-framework aluminophosphate (AlPO) are a family of crystalline materials with uniform pores and channels/cages, and have been widely studied due to their structure diversity and potential applications in catalysis and gas adsorption/separation.[1–4] The open-framework AlPOs could be classified into two categories, according to the electrostatic properties of the associated framework: (i) neutral-framework $AlPO_4$ molecular sieves with equal Al and P atoms, and (ii) anionic AlPO frameworks with an Al/P ratio differing from unity. Various framework Al/P ratios, such as 1/2, 2/3, 3/4, 3/5, 4/5, 5/6, 11/12, 12/13, and 13/18, are found for the anionic AlPO compounds.[5–9]

Typically, the synthesis of AlPO materials generally involves the addition of organic compounds as structure-directing agents (SDAs) or templates.[10–13] An obvious drawback of this strategy is the environmental issues associated with the problematic disposal of the organic containing liquid. Moreover, the high temperature combustion removal of the organic templates is an energy intense process. Besides, the structures of the anionic AlPO could be damaged upon the calcination removal of the occluded organic template. Consequently, to develop an environmentally benign and low-cost organic-free synthesis route is highly desirable for the practical applications of AlPOs. Although various aluminosilicate zeolites, including FAU,[14] ABW,[15] LEV,[16] beta,[17,18] ZSM-34,[19–21] FER,[22] EMT,[23,24] *etc.*,[25,26] are synthesized by employing alkali/alkaline earth cations or by seed-induced approaches, examples of successful AlPO crystalline materials in the absence of organic template remains rare. Continuous efforts have been devoted to the organic-free synthesis of AlPO materials.[15,27–33] Wang *et al.* developed an organotemplate-free method for the synthesis of zeolitic materials in the $Al_2O_3$–$P_2O_5$–$Na_2O$–$H_2O$ system, and an AlPO material of the AEN zeotype structure with the nominal composition of $Na(H_2O)_2|[(AlPO_4)_3OH$ was prepared.[32] Afterwards, the synthesis of a new magnesium alu-

[a]National Engineering Laboratory for Methanol to Olefins, Dalian National Laboratory for Clean Energy, Dalian Institute of Chemical Physics, Chinese Academy of Sciences, Dalian 116023, PR China
[b]Normandie Université, ENSICAEN, UNICAEN, CNRS, CRISMAT, 14000 Caen, France
[c]Normandie Université, ENSICAEN, UNICAEN, CNRS, Laboratoire Catalyse et Spectrochimie, 14000 Caen, France. E-mail: valentin.valtchev@ensicaen.fr
[d]University of Rouen, SMS Laboratory – UPRES EA 3233, 76821 Mont-Saint-Aignan, France
[e]University of Rouen, Laboratoire SMS, Centre Universitaire d'Evreux, 27002 Evreux Cedex, France

†Electronic supplementary information (ESI) available. See DOI: 10.1039/c9qi01223k

minophosphate JU102 with chiral structures was achieved using a similar strategy.[31] By adjusting the synthesis gels and conditions, the same group also succeeded in synthesizing another new open-framework aluminophosphate: $Na_6[(AlPO_4)_8(OH)_6]\cdot 8H_2O$, which possesses excellent proton conductivity.[30] Very recently, Hong *et al.* successfully synthesized a variety of SAPO molecular sieves of high framework charge densities, including MER, EDI, GIS, and ANA type structures, in hydrogels containing different types and concentrations of alkali metal cations without using to OSDAs,[28] although some of these phosphate zeolites have also been obtained by Flanigen and Grose with alkali cations in the early 1970s.[33]

In this work, a novel SAPO material is successfully synthesized in a $Cs^+$ containing hydrogel. The chemical formula of this SAPO is $Cs_2(Al_{0.875}Si_{0.125})_4(P_{0.875}Si_{0.125}O_4)_4(HPO_4)$. The structure of this material is revealed to be iso-structural with $(NH_4)_2Al_4(PO_4)_4(HPO_4)\cdot H_2O$ (AlPO-CJ19),[34] a previously reported aluminophosphate material synthesized using a solvothermal synthesis route, in which pyridine was used as the solvent and 2-aminopyridine as the SDA. From an environmental point of view, the substitution of the organic template by inorganic Cs ions makes the current synthesis protocol more favorable. Moreover, the incorporated $Cs^+$ endows the material with improved thermal stability and high proton/ionic conductivity.

# Experimental section

### Material synthesis

The SAPO material was synthesized using an organic-free method. The employed molar composition of the gel is: $2.2CsOH : 1SiO_2 : 1Al_2O_3 : 2.0P_2O_5 : 120H_2O$. Ultra-stable Y (US-Y) zeolite (CVB720), purchased from Zeolyst and zeolite L, purchased from Tosoh, are used as the silica-alumina source. Prior to the synthesis, zeolite L was subjected to dealumination using 1 M $HNO_3$ acid solution. The solid : liquid ratio was 1 : 40. The zeolite was treated at room temperature for 6 h, and then thoroughly washed with distilled water and dried. Aluminum metal powder and phosphoric acid are chosen as the aluminum and phosphor sources, respectively. A typical synthesis procedure using US-Y includes: (i) 0.25 g USY with a Si/Al ratio of 18.7 was added into 10 grams of CsOH solution (1 M) and the slurry was kept under agitation for 1 h; (ii) 0.216 grams of Al metal powder were added gradually to the slurry and the agitation was continued until the total reaction dissolution of the Al metals; (iii) 3.2 grams of phosphoric acid solution (50 wt%) were subsequently added dropwise. The synthesis procedure based on the $HNO_3$-treated L zeolite is similar. The syntheses with USY (Si/Al = 18.7) and dealuminated zeolite L (Si/Al = 781) were all performed at 180 °C for 72 h. The resulting solid product is collected and washed thoroughly with distilled water. The samples obtained from the USY and $HNO_3$-treated L zeolite containing system were denoted DFZ-64C and DFZ-64D, respectively.

### Characterization

The powder X-ray diffraction (PXRD) data were measured on a Bruker D8 Advance Vario1 diffractometer equipped with a primary germanium (111) Johansson monochromator ($\lambda K\alpha 1$ = 1.5406 Å) and a Lynx Eye detector. A PXRD diagram was recorded at room temperature between 5 and 130°($2\theta$) with a step of ~0.009°($2\theta$) and a time of 4.7 s per step. We also used a variable divergent slit for a constant illuminated sample length of 4 mm. Temperature-dependent powder X-ray diffraction (TD-PXRD) data were recorded on the same diffractometer with an Anton Paar HTK1200N chamber, under an air atmosphere, every 30 °C until 720 °C. Each diagram was recorded with a constant illuminated length of 6 mm, between 7.5 and 60°($2\theta$) with a step of ~0.014°($2\theta$).

Temperature resolved second harmonic (TR-SHG) measurements were recorded with the following equipment. A Nd:YAG Q-switched laser (Quantel) operating at 1.06 μm was used to deliver up to 360 mJ pulses of 5 ns duration with a repetition rate of 10 Hz. An energy adjustment device made up of two polarizers ($P$) and a half-wave plate ($\lambda/2$) allowed the incident energy to vary from 0 to *ca.* 300 mJ per pulse. An RG1000 filter was used after the energy adjustment device to remove the light from laser flash lamps. The samples (few mg of powder in a crucible) were placed in a computer-controlled heating–cooling stage (Linkam THMS-600) and were irradiated with the laser beam (4 mm in diameter). The signal generated by the sample (diffused light) was collected into an optical fiber (500 μm of core diameter) and directed onto the entrance slit of a spectrometer (Ocean Optics). A boxcar integrator allowed an average spectrum (spectral range 490–590 nm) with a resolution of 0.1 nm to be recorded over 3 s (30 pulses). The incident energy was set at *circa* 200 mJ. For temperature resolved measurements, the SHG response was recorded between 20 and 500 °C with a heating rate of 1 °C $min^{-1}$.

One-dimensional (1D) $^{27}Al$ and $^{31}P$ magic-angle spinning nuclear magnetic resonance (MAS NMR) measurements were performed on a Bruker Advance 500 MHz spectrometer using 4 mm $ZrO_2$ rotors. The $^{27}Al$ MAS NMR spectra were recorded under quantitative conditions at a $^{27}Al$ frequency of 130.29 MHz using a short pulse length of 0.77 μs with an RF field of *ca.* 23 kHz, corresponding to the non-selective flip angle of *ca.* π/12, a spinning rate of 12 or 14 kHz and a recycle delay of 1 s. The $^{27}Al$ chemical shifts are reported relative to 1.0 M $Al(H_2O)_6^{3+}$ solution. The $^{31}P$ MAS NMR spectra were recorded at 130.29 MHz with a pulse length of 5.0 ms, a recycle delay of 60 s and the addition of about 3000 pulse transients. $^1H$–$^{31}P$ cross polarization (CP) MAS NMR spectroscopy was carried out with a contact time of 3 ms and a recycle delay of 2 s. The $^{31}P$ chemical shift is reported relative to 0.1 M $H_3PO_4$. All 1D NMR spectral decomposition and simulation were performed using the PeakFit curve-fitting program. The two-dimensional (2D) $^{27}Al$ multiple-quantum (MQ) MAS NMR spectra were recorded at 104.26 MHz on a Bruker Avance 400 spectrometer (9.4 T) using a 4 mm MAS probehead. The MAS NMR spectra were recorded using a pulse length of 1.3 ms

 

with an RF field of *ca.* 30 kHz, corresponding to the non-selective flip angle of *ca.* $p/12$, and a recycle delay of 0.2 s. For MQ MAS, the multiplex spam z-filter pulse method was used as it was shown to produce fast and high-quality spectra. The detailed procedure used in this method was described elsewhere.[35,36] The initial excitation and conversion hard pulse lengths were 2 and 0.8 ms with an RF field of 160 kHz, respectively. The soft pulse was 9 ms with an RF field of 30 kHz.

Elemental compositions were measured by inductively coupled plasma-atomic emission spectroscopy (ICP-AES) using an OPTIMA 4300 DV (Perkin–Elmer) instrument. A MIRA-LMH (Tescan) scanning electron microscope equipped with a field emission gun was employed to obtain the SEM images. TGA/DTA measurements of the samples were carried out using a SETSYS 1750 CS evolution instrument (SETARAM). 15 mg of the sample was heated from 25 to 800 °C with a ramp rate of 5 °C $min^{-1}$ under an air atmosphere (flow rate: 40 mL $min^{-1}$). *In situ* temperature-dependent Fourier transform infrared (FTIR) analyses were carried out on a NICOLET 5700 FT-IR spectrometer equipped with a TGS detector. The self-supporting disk (20 mg, 15 mm in diameter) of the sample was placed in an IR cell attached to a conventional vacuum system. The IR spectra were recorded on the sample after thermal treatment at different temperatures with 128 scans at 4 $cm^{-1}$ of resolution. UV-vis absorption spectra of the cobalt and copper exchanged zeolite powders were recorded using a Varian Cary 4000 spectrophotometer.

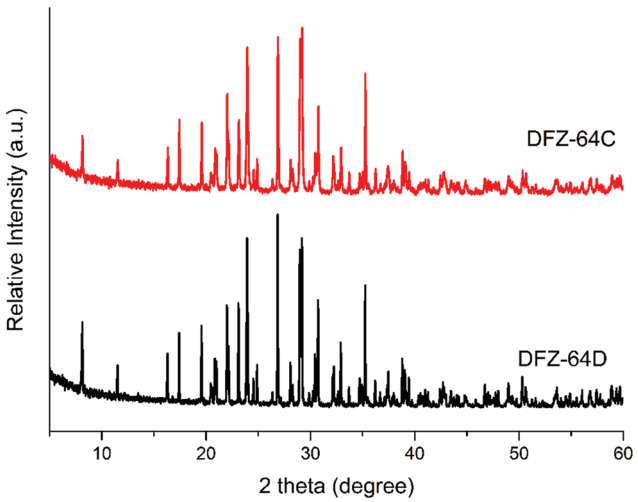


**Fig. 1** XRD patterns of the as-synthesized samples.

### A.C. impedance spectroscopy

The as-synthesized powder was pressed into a self-supporting disk under a force of 1 MPa. Then the sample disk was sealed with the shells of CR2016 coin cells. Electrochemical impedance spectroscopy (EIS) of the coin cell was carried out from $1.0 \times 10^6$ to $1.0 \times 10^4$ Hz at open-circuit voltage with an amplitude of 10 mV on Solartron 1287 and Solartron 1260 electrochemical stations. Therefore, the ionic conductivity of the sample ($\sigma$) was calculated using the ohmic resistance of the coin cell ($R$) and the calculation equation: $\sigma = l/RA$, where $l$ and $A$ stand for thickness and surface area of the sample plate, respectively. It is notable that the ohmic resistance of the coin cell was obtained by fitting with a Zview software, and the thickness and surface area of the sample plate was measured as 0.16 cm and 2.0 $cm^2$, respectively.

## Results and discussion

A crystalline phase with well-resolved XRD diffractions is prepared from the reaction mixture with an optimal composition of $2.2CsOH : 1SiO_2 : 1Al_2O_3 : 2.0P_2O_5 : 120H_2O$ (Fig. 1). All peaks are well resolved, revealing the good crystallinity of the material. No halo due to the existence of amorphous residues could be discerned in the XRD patterns.

SEM images of the prepared SAPO materials are presented in Fig. 2. Two morphologies could be observed for the synthesized samples. DFZ-64D synthesized using the $HNO_3$-

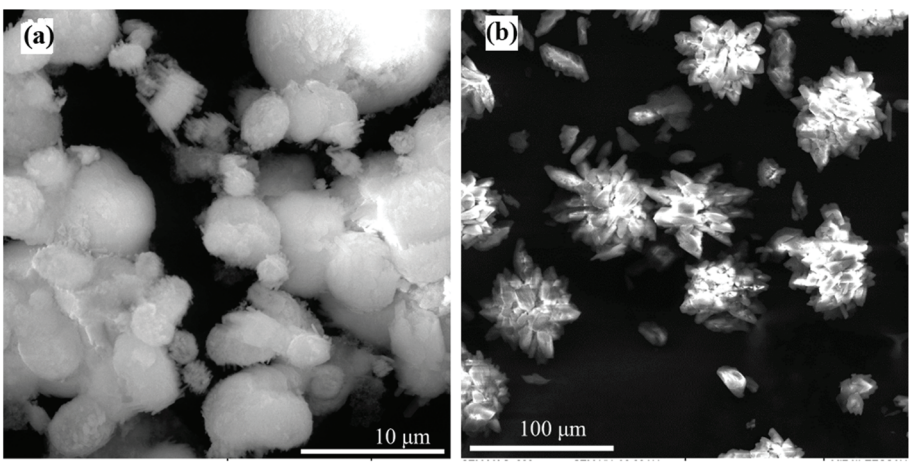


**Fig. 2** SEM images of the as-synthesized samples DFZ-64C (a) and DFZ-64D (b).

treated LTL zeolite as the silicon source possesses the morphology of flower-like assemblies, the size of which locates in the range of 50 to 80 μm. For DFZ-64C synthesized using ultrastable Y as the silicon source, the size of the aggregates is reduced to 5–10 μm, suggesting that the choice of the Si source is crucial in controlling the morphologies of this material. This might be due to the different Si incorporation degrees of the two samples. The elemental compositions of the two as-synthesized samples are determined by ICP-AES analysis. And the elemental compositions are calculated to be $Cs_{0.17}Al_{0.32}P_{0.38}Si_{0.13}$ for DFZ-64C and $Cs_{0.20}Al_{0.33}P_{0.43}Si_{0.05}$ for DFZ-64D. The preferred crystallization temperature is 180 °C. Crystallization could be carried out under either static or tumbling conditions. When the crystallization is carried out at lower temperatures, only a dense phase without well-defined crystalline structures is obtained.

### Structure analysis

The PXRD diagram of DFZ-64C-LT at 20 °C (the low-temperature (20 °C) form of DFZ-64C, Fig. 3) was indexed with the program DICVOL06[37] in a monoclinic unit cell with the following parameters: $a$ = 5.09051(1) Å, $b$ = 21.75661(6) Å, $c$ = 8.22408(2) Å, and $\beta$ = 90.4280(2)°. A whole profile matching of the PXRD diagram was performed with the JANA2006 program[38,39] with the $P2$ space group. A careful observation of the extinction conditions evidences the $P2_1$ or $P2_1/m$ space groups. A Second Harmonic Generation (SHG) qualitative test was performed on a white powder sample of DFZ-64C, in reflection configuration. A notable SHG signal was observed, which proved that the crystal structure of this compound is non-centrosymmetric.[40] The structure was then solved *ab initio* with the SUPERFLIP program[41] which gave a solution in the non-centrosymmetric space group $P2_1$. A first model was obtained without the Si atom. The Rietveld refinements were performed with the JANA2006 program with the fundamental parameter approach.

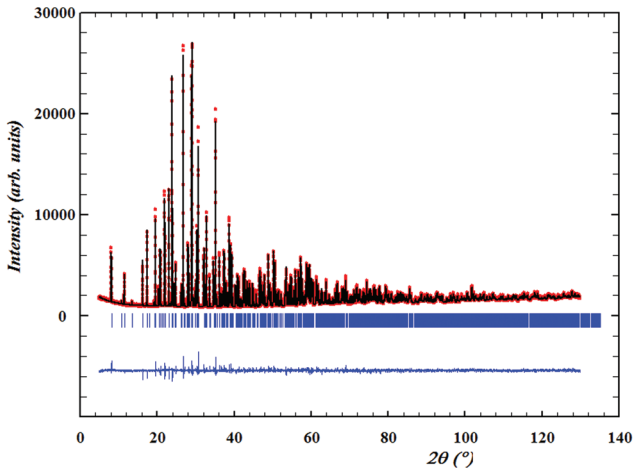


Fig. 3 PXRD diagram of DFZ-64C-LT at 20 °C (Cu-Kα1 radiation; 1.5406 Å) with observed (dots), calculated (solid line), Bragg reflections (ticks), and difference profiles (bottom line) obtained after Rietveld refinements.

The preferential orientation along the [010] direction was taken into account assuming the March & Dollase function. All the atomic positions and isotropic displacement parameters ($U_{iso}$) were refined. The bond valence sums (BVS)[42] calculated with parameters provided by Brese and O'Keeffe[43] showed a lack of electronic charge on the O2 atom. This indicated the presence of a hydrogen atom bonded to O2. This hydrogen atom was geometrically added with distance and angle restraints. There was also a lack of electronic charge on the P5 position and an excess of electronic charge on the Al3 atom positions. Mixed 0.5P/0.5Si and 0.5Al/0.5Si occupancies were taken into account for the P5 and Al3 positions, which corresponded to the expected chemical formula $Cs_2(Al_{1-x}Si_x)_4(P_{1-x}Si_xO_4)_4(HPO_4)$ with $x$ = 0.125. Nevertheless, if the mixed occupancy 0.5P/0.5Si of the "P5" position is quite sure, it can be excluded that the other Si amount is statistically spread over all Al crystallographic sites. The final reliability factors obtained after the last refinement cycle are: $R_{Fobs}$ = 3.19% and $R_{wp}$ = 4.35%. All refinement and crystallographic parameters of DFZ-64C are summarized in Table 1. The atomic positions, the $U_{iso}$ parameters and the bond valence sums (BVS)[42] are presented in ESI Table S1.† A selection of interatomic distances of DFZ-64C is shown in Table 2.

The structure projection of DFZ-64C is shown in Fig. 4. Sample DFZ-64C is revealed to be isostructural with $(NH_4)_2Al_4(PO_4)_4(HPO_4)\cdot H_2O$. Both structures correspond to an open framework base on [$AlO_4$], [$AlO_5$], [$AlO_6$], [$PO_4$] and [$PO_3OH$] polyhedra. Compared with $(NH_4)_2Al_4(PO_4)_4(HPO_4)\cdot H_2O$, the charge of macro-anion $[(Al_{4-x}Si_x)(P_{1-x}Si_xO_4)_4(HPO_4)]^{2-}$ for DFZ-64C is counterbalanced by two $Cs^+$ cations. On the four crystallographic Al positions, Al4 and the mixed Al/Si3 atoms are in tetrahedral coordination [$(Al/Si)O_4$]. The Al–O distances for Al4 range between 1.72(1) and 1.76(1) Å with an average distance of 1.75 Å, which is the same as the one in $(NH_4)_2Al_4(PO_4)_4(HPO_4)\cdot H_2O$. For Al/Si3 the Al–O distances range between 1.67(1) and 1.78(1) Å. The corresponding average distance of 1.72 Å is comparable to that of 1.74 Å observed in $(NH_4)_2Al_4(PO_4)_4(HPO_4)\cdot H_2O$ with a difference of 0.02 Å. The two remaining Al atoms are in trigonal pyramid coordination [$Al2O_5$] (Al–O bond distances: 1.77(1)–1.88(1) Å) and in octahedral coordination [$Al1O_6$] (Al–O bond distances: 1.81(1)–1.95(1) Å). The respective average distances $d_{Al-O-moy}$ are 1.82 and 1.88 Å, in accordance with those in $(NH_4)_2Al_4(PO_4)_4(HPO_4)\cdot H_2O$ of 1.83 and 1.90 Å. All [$AlO_x$] polyhedra are isolated from each other by the [$PO_4$] tetrahedra with which they share O atoms. All the P atoms are in tetrahedral coordination [$PO_4$]. The tetrahedra of the P1, P2, P4, and P5 atoms share all O apexes with adjacent Al atoms. For the P/Si5 mixed atom, the P/Si–O distances range between 1.56(1) and 1.61(1) Å with an average distance of 1.58 Å, which is 0.05 Å bigger than the one in $(NH_4)_2Al_4(PO_4)_4(HPO_4)\cdot H_2O$. For P1, P2 and P4 (P–O bond distances: 1.48(1)–1.6(1) Å), the average P–O distances are 1.55, 1.53 and 1.54 Å, respectively, in agreement with the values observed in $(NH_4)_2Al_4(PO_4)_4(HPO_4)\cdot H_2O$ (1.53, 1.53 and 1.52 Å). The [$P3O_4$] tetrahedra

 

**Table 1** Details of PXRD diagrams and Rietveld refinements of DFZ-64C-LT at 20 °C and DFZ-64C-HT at 570 °C (the high temperature form (570 °C) of DFZ-64C)

| | | | |
|---|---|---|---|
| Diffractometer | Bruker D8 Advance Vario1 Cu-K$\alpha_1$ radiation $\lambda$ = 1.5406 | | |
| Radiation (Å) | | | |
| **Temperature (°C)** | **20** | **570** | |
| 2$\theta$-Range/step (°) | 5–129.997/~0.009 | 10–126.181/~0.012 | |
| **Phase** | **DFZ-64C-LT** | **DFZ-64C-HT** | **$AlPO_4$** |
| Space group | $P12_11$ | $P11b$ | $P63mc$ |
| $Z$ | 2 | 2 | 2 |
| $a$ (Å) | 5.093345(13) | 5.13528(5) | 5.10028(4) |
| $b$ (Å) | 21.76885(5) | 21.8182(2) | 5.10028(4) |
| $c$ (Å) | 8.22861(2) | 8.29896(9) | 8.3375(7) |
| $\beta$ (°) | 90.4280(2) | 89.327(1) | |
| $V$/Å$^3$ | 912.332(4) | 929.77(2) | |
| Molar mass (g mol$^{-1}$) | 848.7 | 848.7 | |
| Mass concentration (%) | 100 | 96.8(1) | 3.2(1) |
| Rietveld refinement: | | | |
| Shape | Pseudo-Voigt | Pseudo-Voigt | |
| Background | 10 Legendre polynomials | 20 Legendre polynomials | |
| Preferred orientation | March & Dollase; $b$-axis | March & Dollase; $c$-axis | |
| Asymmetry | Fundamental parameter | Fundamental parameter | |
| Anisotropic reflection broadening | — | Stephens | |
| Rietveld agreement indices | | | |
| $R_{Fobs}$ | 0.0320 | 0.0361 | 0.0515 |
| $R_{Bobs}$ | 0.0547 | 0.0583 | 0.0983 |
| $R_{wp}$ | 0.0436 | 0.0492 | |
| $cR_{wp}$ | 0.1051 | 0.1451 | |
| Gof | 1.83 | 2.18 | |

**Table 2** Selected interatomic distances for DFZ-64C-LT at 20 °C and DFZ-64C-HT at 570 °C (both polymorphs of $Cs_2(Al_{0.875}Si_{0.125})_4(P_{0.875}Si_{0.125}O_4)_4(HPO_4)$)

| Atom 1 | Atom 2 | Distances (Å) | | Atom 1 | Atom 2 | Distances (Å) | |
|---|---|---|---|---|---|---|---|
| | | DFZ-64C-LT | DFZ-64C-HT | | | DFZ-64C-LT | DFZ-64C-HT |
| Al1 | O10 | 1.90(1) | 1.77(3) | P1 | O10 | 1.48(1) | 1.44(3) |
| | O12 | 1.85(1) | 1.70(3) | | O12 | 1.52(1) | 1.70(3) |
| | O13 | 1.92(1) | 2.16(3) | | O18 | 1.58(1) | 1.59(3) |
| | O4 | 1.81(1) | 1.92(3) | | O9 | 1.61(1) | 1.66(2) |
| | O7 | 1.87(1) | 1.92(3) | P1–O average | | 1.55 | 1.60 |
| | O8 | 1.95(1) | 1.96(3) | P2 | O1 | 1.59(1) | 1.84(3) |
| Al1–O average | | 1.88 | 1.91 | | O11 | 1.55(1) | 1.47(3) |
| Al2 | O16 | 1.86(1) | 1.83(3) | | O15 | 1.49(1) | 1.16(3) |
| | O19 | 1.77(1) | 1.78(3) | | O5 | 1.48(1) | 1.46(3) |
| | O3 | 1.83(1) | 1.84(3) | P2–O average | | 1.53 | 1.48 |
| | O5 | 1.88(1) | 1.96(3) | P3 | O13 | 1.51(1) | 1.54(3) |
| | O9 | 1.78(1) | 1.74(3) | | O16 | 1.48(1) | 1.49(3) |
| Al2–O average | | 1.82 | 1.83 | | O2 | 1.65(1) | 1.73(2) |
| Al/Si3 | O1 | 1.68(1) | 1.48(3) | | O7 | 1.43(1) | 1.36(3) |
| | O14 | 1.74(1) | 1.75(3) | P3–O average | | 1.52 | 1.53 |
| | O15 | 1.78(1) | 2.17(3) | P4 | O14 | 1.61(1) | 1.50(3) |
| | O17 | 1.67(1) | 1.63(2) | | O19 | 1.54(1) | 1.56(2) |
| Al/Si3–O average | | 1.72 | 1.76 | | O3 | 1.51(1) | 1.58(3) |
| Al4 | O11 | 1.76(1) | 1.79(3) | | O8 | 1.51(1) | 1.58(2) |
| | O18 | 1.76(1) | 1.59(3) | P4–O average | | 1.54 | 1.56 |
| | O20 | 1.76(1) | 1.68(3) | P/Si5 | O17 | 1.57(1) | 1.52(2) |
| | O6 | 1.72(1) | 1.94(3) | | O20 | 1.59(1) | 1.57(3) |
| Al4–O average | | 1.75 | 1.75 | | O4 | 1.61(1) | 1.57(2) |
| | | | | | O6 | 1.56(1) | 1.45(3) |
| | | | | P/Si5–O average | | 1.58 | 1.53 |

share two O apexes with Al1 (P3–O bond distances: 1.43(1) and 1.51(1) Å) and one O apex with Al2 (P3–O16 bond length: 1.48(1) Å). The last O apex corresponds to a terminal OH–group, which points to the center of one of the two eight-sided tunnels (P3–O2 bond length: 1.65(1) Å). Both tunnels are delimited by an alternation of [$AlO_x$] and [$PO_4$] polyhedra in the ($bc$) plane. The two $Cs^+$ cations reside in these tunnels merely with weak van der Waals interactions, since the smallest Cs–O distances are calculated to be 3.06(1) Å for Cs1 and 3.10(1) Å for Cs2.

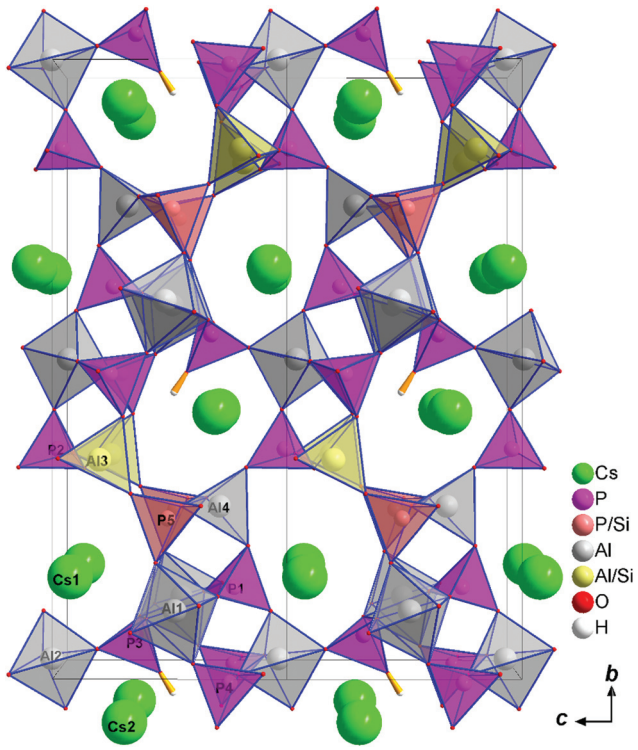


Fig. 4 Structure projection of the (*bc*) plane; 8-MR channels occupied by $Cs^+$ cations are observed along the *a* axis.

The coordination status of the framework species of DFZ-64C is further probed using MAS NMR techniques (see Fig. 5). The $^{27}$Al MAS NMR spectra exhibit three resonance peaks at 42.5, 10 and −17.5 ppm, which could be assigned to tetra-, penta- and hexa- coordinated [$AlO_4$], [$AlO_5$] and [$AlO_6$] species, respectively. Deconvolution results reveal that the relative content of [$AlO_4$], [$AlO_5$] and [$AlO_6$] is in an approximate ratio 2/1/1. Note that the second-order quadrupolar interactions experienced by the half-integer quadrupolar nuclei could alter the resonance signals in the 1d $^{27}$Al MAS NMR spectra. The 2D MQ MAS technique was employed to eliminate the second-order quadrupolar interaction and the corresponding spectra are presented in Fig. 5. In the isotropic (F1) dimension, four peaks could be unambiguously identified. The two peaks with relatively lower chemical shifts correspond to the [$Al2O_5$] and [$Al3O_6$] species, which is congruent with the 1d Al MAS results. The adjacent two peaks at higher chemical shifts in the F1 dimension should be ascribed to the tetracoordinated [$AlO_4$] species at different crystallographic Al sites. This is in good congruence with the structure solution results in the previous sector, which shows that two crystallographic sites co-exist for the tetra-coordinated Al1 species and mixed Al/Si4 sites.

The phosphorus atom coordination environments are probed by the $^{31}$P MAS NMR technique and the corresponding spectrum is shown in Fig. 6. The deconvolution of the spectrum reveals that the curve comprises five independent resonance peaks, centered at −21.7, −22.7, −25.1, −26.7 and −29.5 ppm, which corresponds to the tetragonal [$PO_4$] species at the five crystallographic phosphor sites, respectively. Moreover, the relative ratio of the five tetragonal [$PO_4$] species is calculated to be around 0.23 : 0.21 : 0.16 : 0.24 : 0.17. The deviation from unity might be explained by the fact that in some position P is partially replaced with Si, which is also well supported by the crystallographic analysis. The $^{1}$H–$^{31}$P CP MAS NMR spectrum of the sample is also collected and shown in Fig. 6. The resonance peak at −21.7 ppm is significantly enhanced in the CP MAS spectra, indicating that the peak at −21.7 ppm corresponds to the P5 site linked with the terminal hydroxyl groups revealed in the structure analysis results.

## Thermal stability

Thermal stability is an important property influencing the potential applications of the open-framework aluminopho-

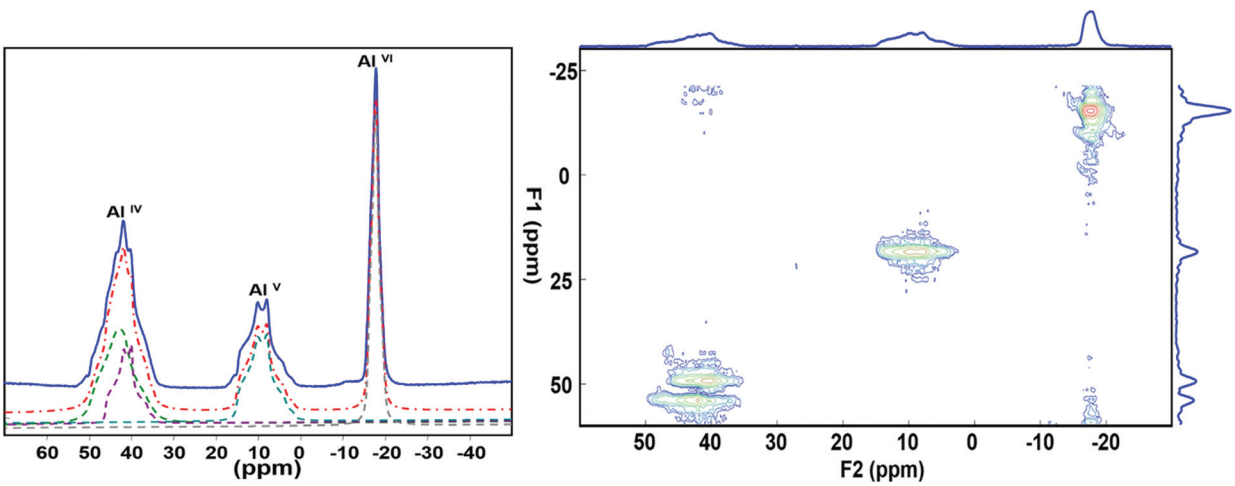


Fig. 5 1d $^{27}$Al MAS NMR spectra (left) and 2d $^{27}$Al MQ MAS NMR spectra (right) of sample DFZ-64C.

 

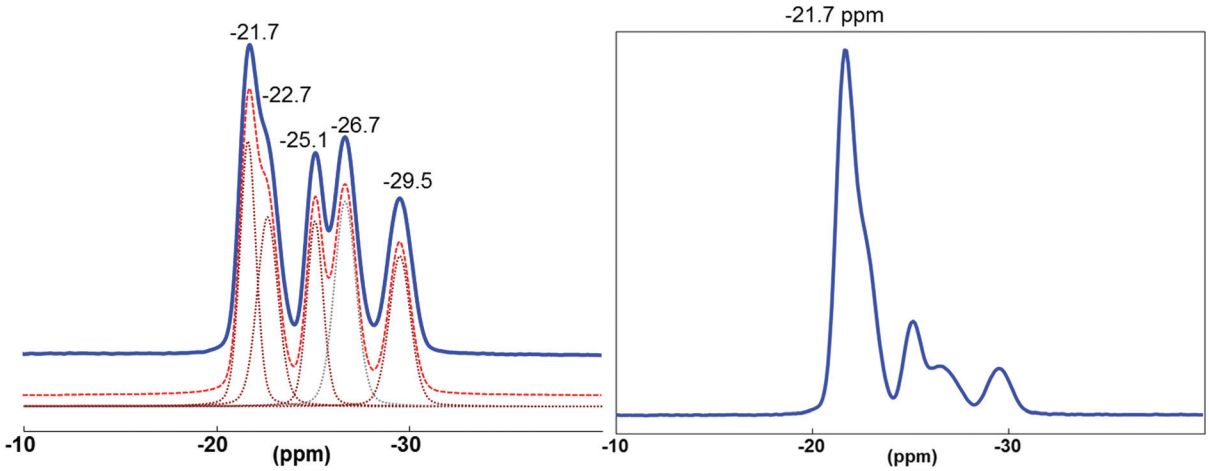


Fig. 6 $^{31}P$ MAS (left) and $^{1}H-^{31}P$ CP MAS NMR spectra (right) of sample DFZ-64C.

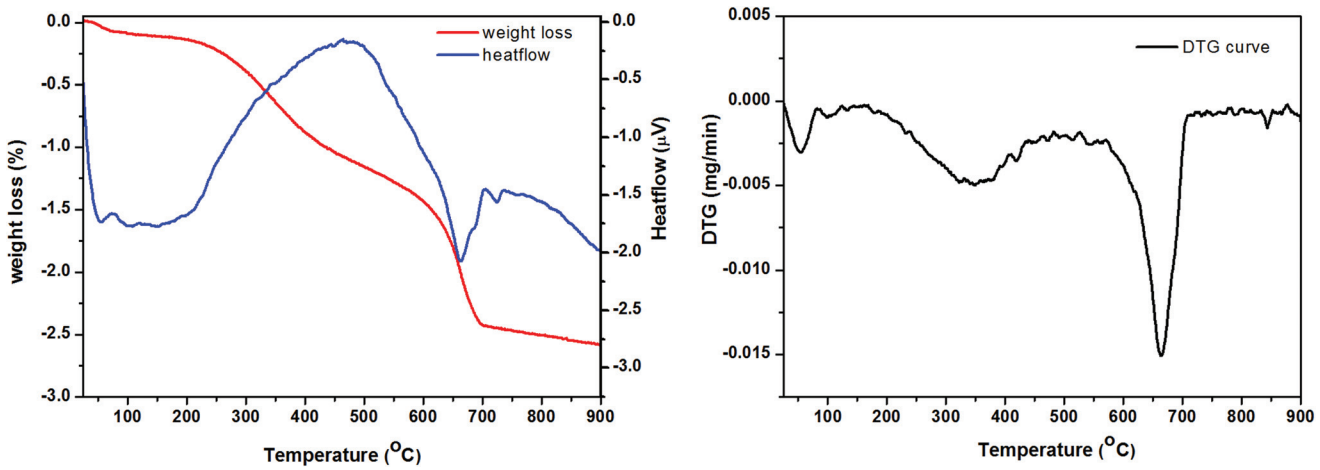


Fig. 7 TG-DSC analysis curves of sample DFZ-64C: TGA and heat flow curves (left) and DTG curve (right).

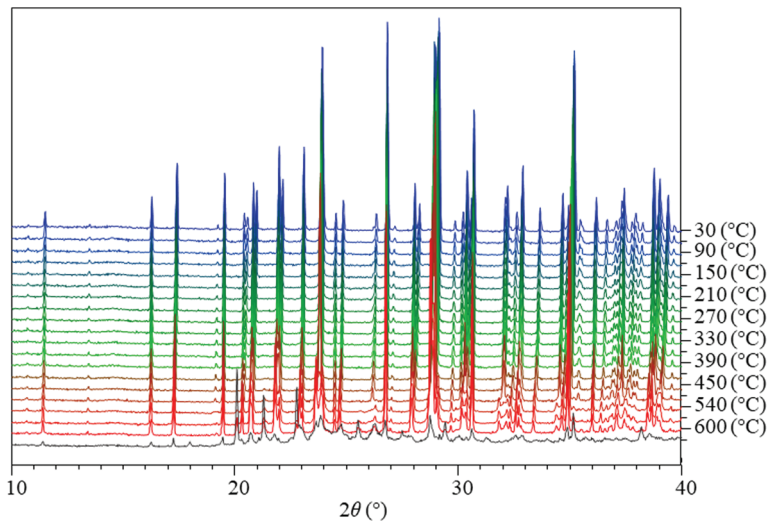


Fig. 8 Temperature-programmed *in situ* XRD patterns of sample DFZ-64C.

sphate materials. As mentioned in the XRD analysis, the XRD patterns of the material show no significant variation after calcination at 550 °C. This phenomenon is quite different from its aluminophosphate counterpart $(NH_4)_2Al_4(PO_4)_4(HPO_4)\cdot H_2O$, denoted as AlPO-CJ19.[34] A comprehensive analysis is further carried out to investigate the thermal behavior and phase transformation phenomenon of the material, using combined technologies of TG-DSC, temperature-programed *in situ* XRD and *in situ* temperature-dependent FTIR analysis.

The TGA curve reveals a continuous weight loss of merely 1.8 wt% from room temperature to around 600 °C, due to the thermal desorption of the incorporated water molecules (Fig. 7). This is quite different from the typical TGA curves of the organic-incorporated aluminophosphate materials, for which significant weight losses due to the combustion removal of the occluded organics are generally observed. In fact, the weight loss curve between 200 and 600 °C is clearly composed of two different weight losses (before and after 400 °C), corresponding to the removal of the weakly bonded and strongly bonded water molecules, respectively. Another notable weight loss of around 1 wt% is observed in the temperature range between 600 and 700 °C (also evidenced by the presence of the sharp peak in the DTG curve), accompanied by an obvious endothermic peak. This weight loss is associated with the framework collapse and decomposition of the material.

The phase transition of the sample is monitored by temperature-programmed *in situ* XRD analysis and the corresponding XRD patterns are shown in Fig. 8. Below 510 °C, the positions and intensities of the XRD patterns show no variation, suggesting that the structure of the framework is rather

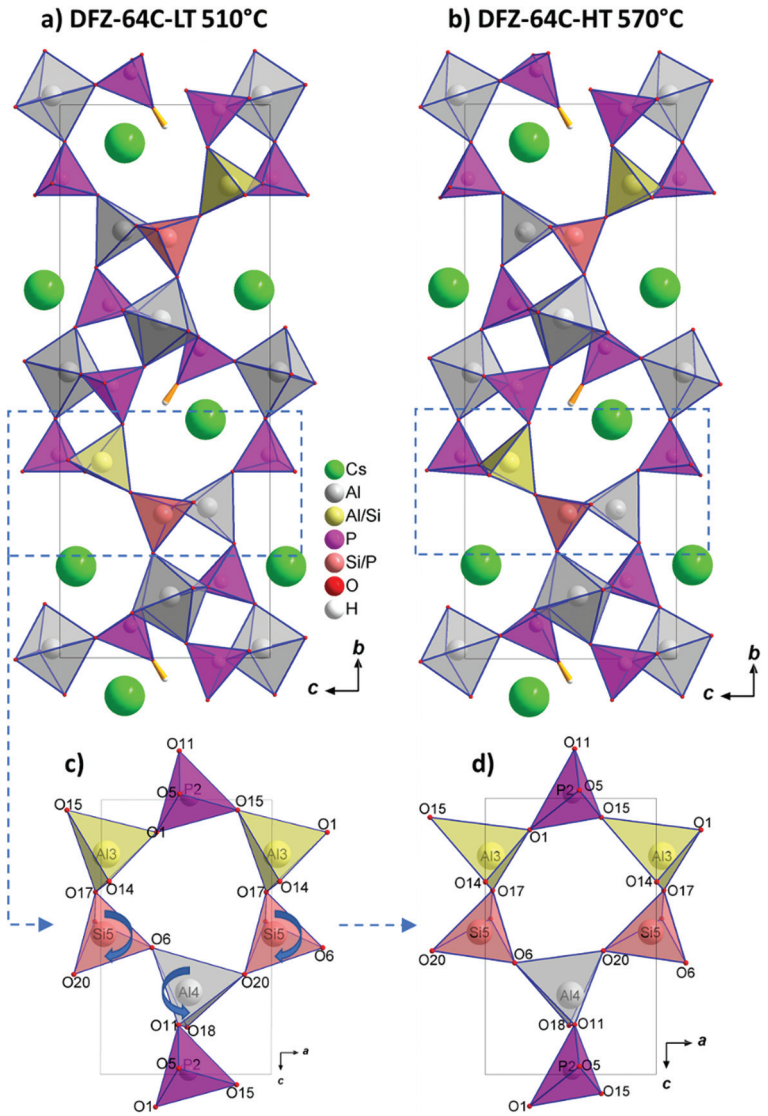


**Fig. 9** Views of the structures of $Cs_2(Al_{0.875}Si_{0.125})_4(P_{0.875}Si_{0.125}O_4)_4(HPO_4)$ polymorphs (a) DFZ-64C-LT at 510 °C and (b) DFZ-64C-HT at 570 °C after the transition. Bottom figures (c) and (d) show the displacement of the oxygen atoms between the two polymorphs for part of the structural framework. The blue arrows in the LT structure indicate how the [$Si5O_4$] and [$Al4O_4$] tetrahedra must rotate around the *b* axis to form the HT structure.

 

stable and barely perturbed by the thermal treatment below 510 °C. However, upon increasing the temperature to 540 °C, a phase transition between two polymorphs of $Cs_2(Al_{0.875}Si_{0.125})_4(P_{0.875}Si_{0.125}O_4)_4(HPO_4)$ is evidenced. For clarity, the two polymorphs are denoted as DFZ-64C-LT for the low-temperature form and DFZ-64C-HT for the high-temperature form, respectively. The structures of both polymorphs (DFZ-64C-LT at 510 °C and DFZ-64C-HT at 570 °C) are resolved and depicted in Fig. 9. Both structures are monoclinic: the phase DFZ-64C-LT at 510 °C crystallizes in the $P2_1$ space group and its high temperature counterpart crystallizes in $P11b$. This non-conventional setting was chosen to conserve the same *a*, *b* and *c*-axis for both structures. Again, a notable SHG signal was observed at 540 °C, which proved that the crystal structure of this HT-phase is also non-centrosymmetric (Fig. S3†). Both space groups are polar and non-centrosymmetric but there are no group–subgroup relations between the two structures meaning this transition is of first-order. The structure was solved *ab initio* against PXRD data at 570 °C in the $P11b$ space group with the SUPERFLIP program. Rietveld refinements were performed with JANA2006 (Fig. s2†). Anisotropic peak broadening was taken into consideration using the Stephens model.[44] Indeed, the phase transformation implies a strong compression along the *b*-axis which decreases from 21.9 Å at 510 °C to 21.8190(2) Å at 570 °C (Fig. 10). In parallel $\beta$ reduces to 90° while $\gamma$ is reduced from 90 to 89.3276°. This strong anisotropic strain in phase $Cs_2(Al_{0.875}Si_{0.125})_4(P_{0.875}Si_{0.125}O_4)_4(HPO_4)$-HT also explains the decreasing of the SHG signal (see Fig. s1†). Note that the sample also undergoes a slight decomposition with the appearance of the $AlPO_4$ phase during the phase transition. All refinement and crystallographic parameters of DFZ-64C-HT at 570 °C are summarized in Table 1. The atomic positions and $U_{iso}$ are presented in Table 2. A selection of interatomic distances of DFZ-64C-HT at 570 °C is shown in Table 2. Finally, after the temperature is above 600 °C, the sample decomposes into $SiO_2$, $AlPO_4$, and $CsPO_3$, which is congruent with the TG-DSC results revealing the occurrence of the framework decomposition in the same temperature range.

If one compares the structures of two polymorphs just before and above the transition at 510 and 570 °C (Fig. 9) it can be seen that the open framework based on $[AlO_4]$, $[AlO_5]$, $[AlO_6]$, $[PO_4]$ and $[PO_3OH]$ polyhedra is conserved. The loss of the $2_1$ axis along the *b*-axis is replaced by the *b* glide-plan perpendicular to the *c*-axis. This transformation essentially involves oxygen atom displacements while the cations stay roughly on the same positions. All average P–O and Al–O distances in DFZ-64C-HT at 570 °C are comparable to those observed previously in DFZ-64C-LT at 20 °C (Table 2).

The hydroxyl functional groups are of particular interest for the applications of porous materials. *In situ* FTIR techniques are used to identify and follow the variation of the –OH groups with the ramp of temperature (Fig. 10). Four absorptions at around 3743, 3659, 3571 and 3456 $cm^{-1}$ could be observed. The peak at 3743 $cm^{-1}$ is ascribed to the hydroxyls attached to the crystal surfaces. The peaks at 3659 and 3571 $cm^{-1}$ are speculated to arise from water molecules weakly hydrogen-bonded to the aluminum and phosphor species in the defect sites. With the increase of temperature, the intensities of the two peaks diminish gradually and disappear completely above 350 °C, suggesting the complete removal of the weakly adsorbed water molecules, which corresponds well to the first weight loss in the TG analysis. The hydroxyls corresponding to the absorption peak at 3456 $cm^{-1}$ is rather stable. Below 450 °C, no significant decrease in the peak at 3456 $cm^{-1}$ could be discerned. After thermal treatment at 550 °C, only a tiny decrease could be observed. These hydroxyls with relatively higher thermal stability are speculated to correspond to the –OH groups linked with the framework P species at P5 sites, as revealed by the XRD refinement analysis.

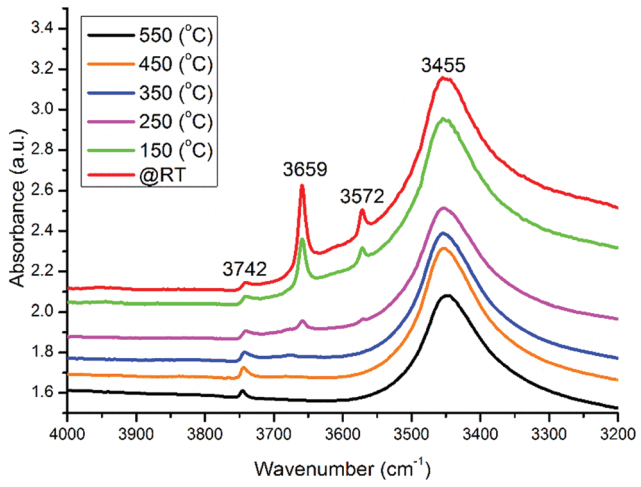


**Fig. 10** Analysis of the –OH stretching mode of sample DFZ-64C by temperature-programmed *in situ* FTIR spectroscopy.

## Ion-exchange properties

The UV-vis absorption spectra of cobalt and copper exchanged samples are shown in Fig. 11. In the spectra of the $Co^{2+}$ exchanged sample, an absorption peak centered at a wavelength of 526 nm could be observed, which corresponds to the isolated octahedral $Co^{2+}$ cations introduced during the ion exchange process. The light pink color of the powder also suggests that the majority of the exchanged $Co^{2+}$ are in the octahedral coordination status (see Fig. S4†). As for the $Cu^{2+}$ exchanged sample, an absorption at around 553 nm is observed, corresponding to the incorporated copper species. Note that this absorption intensifies with the increase of exchange times.

## A.C. impedance analysis

A.C. impedance spectroscopy is employed to test the ion/proton conductivity of this material at room temperature. The corresponding A.C. impedance plots are illustrated in Fig. 12. The ion/proton conductivity is calculated to be $1.70 \times 10^{-4}$ S $cm^{-1}$ (293 K, 30% relative humidity), which is one magnitude higher than that of a notable open-framework AlPO material

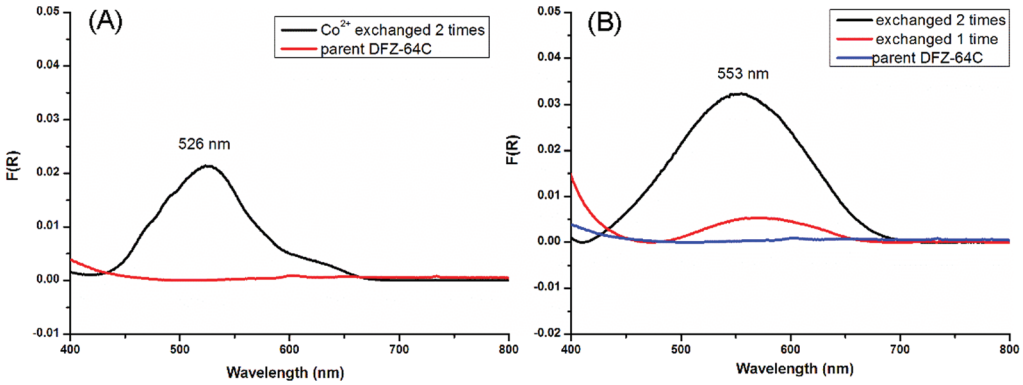


**Fig. 11** The UV-VIS spectra of sample DFZ-64C after $Co^{2+}$ exchange in 0.05 M $Co(Ac)_2$ solution (A, 50 °C, 4 h) and $Cu^{2+}$ exchange in 0.05 M $Cu(Ac)_2$ solution (B, 50 °C, 4 h).

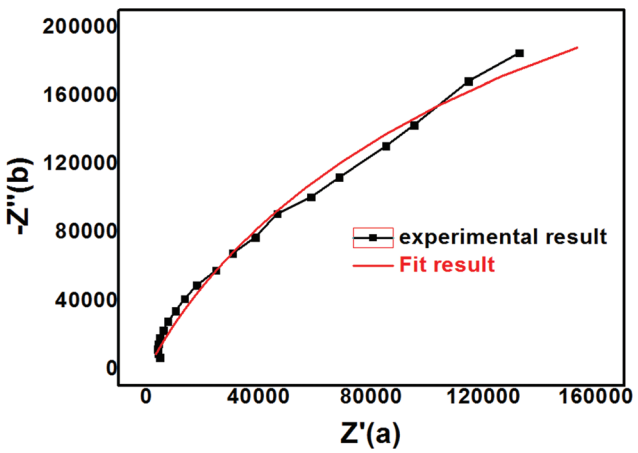


**Fig. 12** A.C. impedance plots of sample DFZ-64C.

JU-103 (around $2.52 \times 10^{-5}$ S $cm^{-1}$, 293 K, 33% relative humidity).[30] As revealed by the previous structure analysis, abundant $Cs^+$ ions, physically adsorbed water and terminal P–OH exist in the structure, which might have endowed the material with this high ionic/proton conductivity.

## Conclusions

In summary, an open-framework SAPO material with the chemical formula of $Cs_2(Al_{0.875}Si_{0.125})_4(P_{0.875}Si_{0.125}O_4)_4(HPO_4)$ was successfully synthesized in a cesium-containing hydrogel system. The material was resolved to be isostructural with an open-framework aluminophosphate (AlPO) material AlPO-CJ19. This is the first report of the successful synthesis of the silicon-containing counterpart of AlPO-CJ19. The incorporation of the Si species could be testified by both the elemental analysis and structure analysis. From an environmental point of view, the utilization of pure inorganic synthesis gel makes the current synthesis protocol more favorable. Besides, the thermal stability of the material is significantly improved due to the substitution of the organic template by inorganic $Cs^+$ cations. UV-vis results reveal that cobalt and copper cations could be readily incorporated through simple ion-exchange treatment. The conductivity of the material is revealed to be $1.70 \times 10^{-4}$ S $cm^{-1}$ (293 K, 30% relative humidity) as revealed by the A.C. impedance spectroscopy analysis, an impressive value for this kind of material. The abundant $Cs^+$ cations and terminal P–OH in this material are the origin of its high ion/proton conductivity.

## Conflicts of interest

There are no conflicts of interest to declare.

## Acknowledgements

The authors acknowledge funding support from the Sino-French joint laboratory “Zeolites”.

## References

1 S. T. Wilson, B. M. Lok, C. A. Messina, T. R. Cannan and E. M. Flanigen, Aluminophosphate Molecular-Sieves - a New Class of Microporous Crystalline Inorganic Solids, *J. Am. Chem. Soc.*, 1982, **104**(4), 1146–1147.
2 S. Mintova, S. Mo and T. Bein, Nanosized AlPO4-5 molecular sieves and ultrathin films prepared by microwave synthesis, *Chem. Mater.*, 1998, **10**(12), 4030–4036.
3 D. Fan, P. Tian, X. Su, Y. Y. Yuan, D. H. Wang, C. Wang, M. Yang, L. Y. Wang, S. T. Xu and Z. M. Liu, Aminothermal synthesis of CHA-type SAPO molecular sieves and their catalytic performance in methanol to olefins (MTO) reaction, *J. Mater. Chem. A*, 2013, **1**(45), 14206–14213.
4 P. Tian, Y. X. Wei, M. Ye and Z. M. Liu, Methanol to Olefins (MTO): From Fundamentals to Commercialization, *ACS Catal.*, 2015, **5**(3), 1922–1938.

 

5 J. H. Yu and R. R. Xu, Insight into the construction of open-framework aluminophosphates, *Chem. Soc. Rev.*, 2006, **35**(7), 593–604.
6 J. H. Yu and R. R. Xu, Rich structure chemistry in the aluminophosphate family, *Acc. Chem. Res.*, 2003, **36**(7), 481–490.
7 J. H. Yu, L. Y. Li and R. R. Xu, Towards rational design and synthesis of aluminophosphates with 2-D layer and 3-D open-framework structures, *Microporous Mesoporous Mater.*, 2001, **48**(1–3), 47–56.
8 W. F. Yan, J. H. Yu, R. R. Xu, G. S. Zhu, F. S. Xiao, Y. Han, K. Sugiyama and O. Terasaki, [Al12P13O52](3-)[(CH2)(6) N4H3](3+): An anionic aluminophosphate molecular sieve with Bronsted acidity, *Chem. Mater.*, 2000, **12**(9), 2517–2519.
9 K. X. Wang, J. H. Yu, Z. Shi, P. Miao, W. F. Yan and R. R. Xu, Synthesis and characterization of a new three-dimensional aluminophosphate [Al11P12O48][C4H12N2] [C4H11N2] with an Al/P ratio of 11 : 12, *J. Chem. Soc., Dalton Trans.*, 2001, (12), 1809–1812.
10 D. Fan, P. Tian, S. T. Xu, D. H. Wang, Y. Yang, J. Z. Li, Q. Y. Wang, M. Yang and Z. M. Liu, SAPO-34 templated by dipropylamine and diisopropylamine: synthesis and catalytic performance in the methanol to olefin (MTO) reaction, *New J. Chem.*, 2016, **40**(5), 4236–4244.
11 C. S. Cundy and P. A. Cox, The hydrothermal synthesis of zeolites: History and development from the earliest days to the present time, *Chem. Rev.*, 2003, **103**(3), 663–701.
12 X. Q. Tong, J. Xu, C. Wang, H. Y. Lu, P. Huang, W. F. Yan, J. H. Yu, F. Deng and R. R. Xu, Molecular engineering of microporous crystals: (V) Investigation of the structure-directing ability of piperazine in forming two layered aluminophosphates, *Microporous Mesoporous Mater.*, 2012, **155**, 153–166.
13 H. Y. Lu, X. Q. Tong, Y. Yan, W. F. Yan, J. H. Yu and R. R. Xu, Synthesis, Structure and Phase Transition of a New Microporous Aluminophosphate [C4N2H14](2+) [H2Al3P3O14](2-), *Chem. Res. Chin. Univ.*, 2013, **34**(7), 1571–1575.
14 H. Awala, J. P. Gilson, R. Retoux, P. Boullay, J. M. Goupil, V. Valtchev and S. Mintova, Template-free nanosized faujasite-type zeolites, *Nat. Mater.*, 2015, **14**(4), 447–451.
15 T. M. A. Ghrear, S. Rigolet, T. J. Daou, S. Mintova, T. C. Ling, S. H. Tan and E. P. Ng, Synthesis of Cs-ABW nanozeolite in organotemplate-free system, *Microporous Mesoporous Mater.*, 2019, **277**, 78–83.
16 H. Y. Zhang, C. G. Yang, L. F. Zhu, X. J. Meng, B. Yilmaz, U. Muller, M. Feyen and F. S. Xiao, Organotemplate-free and seed-directed synthesis of levyne zeolite, *Microporous Mesoporous Mater.*, 2012, **155**, 1–7.
17 B. Xie, J. W. Song, L. M. Ren, Y. Y. Ji, J. X. Li and F. S. Xiao, Organotemplate-free and fast route for synthesizing Beta zeolite, *Chem. Mater.*, 2008, **20**(14), 4533–4535.
18 K. Iyoki, K. Itabashi and T. Okubo, Seed-Assisted, One-Pot Synthesis of Hollow Zeolite Beta without Using Organic Structure-Directing Agents, *Chem. – Asian J.*, 2013, **8**(7), 1419–1427.
19 C. G. Yang, L. M. Ren, H. Y. Zhang, L. F. Zhu, L. Wang, X. J. Meng and F. S. Xiao, Organotemplate-free and seed-directed synthesis of ZSM-34 zeolite with good performance in methanol-to-olefins, *J. Mater. Chem.*, 2012, **22**(24), 12238–12245.
20 L. Zhang, C. G. Yang, X. J. Meng, B. Xie, L. Wang, L. M. Ren, S. J. Ma and F. S. Xiao, Organotemplate-Free Syntheses of ZSM-34 Zeolite and Its Heteroatom-Substituted Analogues with Good Catalytic Performance, *Chem. Mater.*, 2010, **22**(10), 3099–3107.
21 Z. F. Wu, J. W. Song, Y. Y. Ji, L. M. Ren and F. S. Xiao, Organic template-free synthesis of ZSM-34 zeolite from an assistance of zeolite L seeds solution, *Chem. Mater.*, 2008, **20**(2), 357–359.
22 H. Y. Zhang, Q. Guo, L. M. Ren, C. G. Yang, L. F. Zhu, X. J. Meng, C. Li and F. S. Xiao, Organotemplate-free synthesis of high-silica ferrierite zeolite induced by CDO-structure zeolite building units, *J. Mater. Chem.*, 2011, **21**(26), 9494–9497.
23 E. P. Ng, D. Chateigner, T. Bein, V. Valtchev and S. Mintova, Capturing Ultrasmall EMT Zeolite from Template-Free Systems, *Science*, 2012, **335**(6064), 70–73.
24 E. P. Ng, H. Awala, J. P. Ghoy, A. Vicente, T. C. Ling, Y. H. Ng, S. Mintova and F. Adam, Effects of ultrasonic irradiation on crystallization and structural properties of EMT-type zeolite nanocrystals, *Mater. Chem. Phys.*, 2015, **159**, 38–45.
25 M. E. Davis, Zeolites from a Materials Chemistry Perspective, *Chem. Mater.*, 2014, **26**(1), 239–245.
26 X. J. Meng and F. S. Xiao, Green Routes for Synthesis of Zeolites, *Chem. Rev.*, 2014, **114**(2), 1521–1543.
27 Y. Q. Wang, Q. M. Wu, X. J. Meng and F. S. Xiao, Insights into the Organotemplate-Free Synthesis of Zeolite Catalysts, *Engineering-PRC*, 2017, **3**(4), 567–574.
28 S. H. Park, W. Choi, H. J. Choi and S. B. Hong, Organic-Free Synthesis of Silicoaluminophosphate Molecular Sieves, *Angew. Chem., Int. Ed.*, 2018, **57**(30), 9413–9418.
29 R. M. Barrer and D. J. Marshall, Chemistry of soil minerals .I. hydrothermal crystallisation of some alkaline AL2O3-SIO2-P2O5 compositions, *J. Chem. Soc.*, 1965, 6616–6621.
30 Y. J. Sun, Y. Yan, Y. Y. Wang, Y. Li, J. Y. Li and J. H. Yu, High proton conduction in a new alkali metal-templated open-framework aluminophosphate, *Chem. Commun.*, 2015, **51**(45), 9317–9319.
31 Y. Mu, Y. Y. Wang, Y. Li, J. Y. Li and J. H. Yu, Organotemplate-free synthesis of an open-framework magnesium aluminophosphate with proton conduction properties, *Chem. Commun.*, 2015, **51**(11), 2149–2151.
32 Y. Y. Wang, Y. J. Sun, Y. Mu, C. Q. Zhang, J. Y. Li and J. H. Yu, Organotemplate-free hydrothermal synthesis of an aluminophosphate molecular sieve with AEN zeotype topology and properties of its derivatives, *Chem. Commun.*, 2014, **50**(97), 15400–15403.
33 E. M. Flanigen and R. W. Grose, Phosphorus Substitution in Zeolite Frameworks, in *Molecular Sieve Zeolites-I*, American chemical society, 1974, vol. 101, pp. 76–101.

34 D. Zhou, L. Chen, J. H. Yu, Y. Li, W. F. Yan, F. Deng and R. R. Xu, Synthesis, crystal structure, and solid-state NMR Spectroscopy of a new open-framework aluminophosphate (NH4)(2)Al-4(PO4)(4)(HPO4)center dot H2O, *Inorg. Chem.*, 2005, **44**(12), 4391–4397.

35 N. Malicki, L. Mafra, A. A. Quoineaud, J. Rocha, F. Thibault-Starzyk and C. Fernandez, Multiplex MQMAS NMR of quadrupolar nuclei, *Solid State Nucl. Magn. Reson.*, 2005, **28**(1), 13–21.

36 J. P. Amoureux, C. Fernandez and S. Steuernagel, Z filtering in MQMAS NMR, *J. Magn. Reson., Ser. A*, 1996, **123**(1), 116–118.

37 D. Louer and A. Boultif, Indexing with the successive dichotomy method, DICVOL04, *Z. Kristallogr.*, 2006, 225–230.

38 V. Petricek, M. Dusek and L. Palatinus, Crystallographic Computing System JANA2006: General features, *Z. Kristallogr. - Cryst. Mater.*, 2014, **229**(5), 345–352.

39 M. Dusek, V. Petricek and L. Palatinus, Advances in solution of modulated structures reflected by Jana system, *6th International Conference on Aperiodic Crystals (Aperiodic'09)* 2010, 226.

40 S. K. Kurtz and T. T. Perry, A Powder Technique for the Evaluation of Nonlinear Optical Materials, *J. Appl. Phys.*, 1968, **39**(8), 3798–3813.

41 L. Palatinus and G. Chapuis, SUPERFLIP - a computer program for the solution of crystal structures by charge flipping in arbitrary dimensions, *J. Appl. Crystallogr.*, 2007, **40**, 786–790.

42 I. D. Brown, VALENCE: A program for calculating bond valences, *J. Appl. Crystallogr.*, 1996, **29**, 479–480.

43 N. E. Brese and M. O'Keeffe, Bond-Valence Parameters for Solids, *Acta Crystallogr., Sect. B: Struct. Sci.*, 1991, **47**, 192–197.

44 P. Stephens, Phenomenological model of anisotropic peak broadening in powder diffraction, *J. Appl. Crystallogr.*, 1999, **32**(2), 281–289.

 